Land surface skin temperatures from a combined analysis of microwave and infrared satellite observations for an all-weather evaluation of the differences between air and skin temperatures

Catherine Prigent
CNRS, LERMA, Observatoire de Paris, France

Filipe Aires[1] and William B. Rossow
NASA Goddard Institute for Space Studies, New York, New York, USA

Received 14 March 2002; revised 20 January 2003; accepted 6 February 2003; published 24 May 2003.

[1] A neural network inversion scheme including first guess information has been developed to retrieve surface temperature T_s, along with atmospheric water vapor, cloud liquid water, and surface emissivities over land from a combined analysis of Special Sensor Microwave/Imager (SSM/I) and International Satellite Cloud Climatology Project (ISCCP) data. In the absence of routine in situ surface skin measurements, retrieved T_s values are evaluated by comparison to the surface air temperature T_{air} measured by the meteorological station network. The $T_s - T_{air}$ difference shows all the expected variations with solar flux, soil characteristics, and cloudiness. During daytime the $T_s - T_{air}$ difference is driven by the solar insulation, with positive differences that increase with increasing solar flux. With decreasing soil and vegetation moisture the evaporation rate decreases, increasing the sensible heat flux, thus requiring larger $T_s - T_{air}$ differences. Nighttime $T_s - T_{air}$ differences are governed by the longwave radiation balance, with T_s usually closer or lower than T_{air}. The presence of clouds dampens all the difference. After suppression of the variability associated to the diurnal solar flux variations, the T_s and T_{air} data sets show very good agreement in their synoptic variations, even for cloudy cases, with no bias and a global rms difference of ~2.9 K. This value is an upper limit of the retrieval rms because it includes errors in the in situ data as well as errors related to imperfect time and space collocations between the satellite and in situ measurements. *INDEX TERMS:* 0315 Atmospheric Composition and Structure: Biosphere/atmosphere interactions; 3322 Meteorology and Atmospheric Dynamics: Land/atmosphere interactions; 3360 Meteorology and Atmospheric Dynamics: Remote sensing; 1640 Global Change: Remote sensing; *KEYWORDS:* biosphere/atmosphere interactions, land/atmosphere interactions, remote sensing

Citation: Prigent, C., F. Aires, and W. B. Rossow, Land surface skin temperatures from a combined analysis of microwave and infrared satellite observations for an all-weather evaluation of the differences between air and skin temperatures, *J. Geophys. Res.*, *108*(D10), 4310, doi:10.1029/2002JD002301, 2003.

1. Introduction

[2] Skin temperature (T_s) is the physical temperature of the Earth's surface. For more complex situations like vegetated surfaces, the skin temperature can refer to an average effective radiative temperature of the canopy and surface [*Hall et al.*, 1992; *Betts et al.*, 1996]. Oceans are homogeneous over large scales, with nearly constant albedos, high heat capacity, and infinite moisture supply. In contrast, land surfaces are highly variable in space, have lower heat capacity and limited moisture. As a consequence, when exposed to solar flux variations, land skin temperatures not only exhibit stronger diurnal to seasonal variations, they are also more variable in space, modulated by surface properties like vegetation density and soil moisture.

[3] Upwelling longwave radiation from the surface directly depends upon the surface skin temperature T_s. Some General Circulation Models (GCM) compute this variable but it is not conventionally observed by the meteorological weather station network. However air temperatures at 2 m (T_{air}) are routinely measured and for validation purposes climatologies of air temperature [e.g., *Legates and Willmott*, 1990] are often used for comparison with T_s, sometimes confusing air temperature, surface skin temperature, and temperature at the first level of the GCM model [*Garrat*, 1995]. *Garrat* [1995] showed that systematic comparisons of the GCM output T_s with T_{air} without an adequate treatment of the $T_s - T_{air}$ difference (with monthly means up to

[1] Also at Laboratoire de Météorologie Dynamique, École Polytechnique, Palaiseau, France.

0148-0227/03/2002JD002301$09.00

2 K averaged over continents) result in an underestimation of T_s by the GCM models and, as a consequence, an underestimation of the cooling of the surface by longwave fluxes. Thus excess net radiation calculated in GCMs over continents may not be due only to overestimates in incoming shortwave fluxes but also to underestimates in upwelling longwave fluxes related to underestimated T_s [*Garrat*, 1995].

[4] Energy exchanges at the land-surface boundary are largely controlled by the difference between the skin temperature and the surface air temperature, the air and the surface reacting with different time and space scales to external forcing while still being complexly interconnected. The land surface temperature responds more rapidly to changes of the local balance of energy than the air temperature. On the other hand, surface heat fluxes can induce local convection in the boundary layer, producing changes in air temperature, surface winds, cloudiness, and (potentially) precipitation [*Betts and Ball*, 1995]. All of these parameters can also be affected by advection of different air masses into the region. The partition of net radiation at the land surface into latent and sensible heat fluxes, which can be parameterized in terms of the skin - air temperature differences, is a crucial problem spanning all spatial and temporal scales.

[5] Estimates of the surface temperature diurnal cycle can yield information about the soil moisture via an estimate of the thermal inertia. *Idso et al.* [1975] showed that the daily amplitude of the skin temperature and daily maximum of the surface soil minus air temperatures can be used to estimate soil water content and soil evaporation rate. *Price* [1977] and *Carlson et al.* [1981] indicated that thermal inertia and soil moisture can be estimated from two measurements of T_s a day. *Jackson et al.* [1977] suggested making the daily latent heat (or evapotranspiration) minus the net radiation linearly proportional to $(T_s - T_{air})$ at midday, a method that has often been used since. Since 1983, the International Satellite Land Surface Climatology Project (ISLSCP) has sensitized the research community to the key role of land-atmosphere interactions and has stimulated a number of model investigations and measurement campaigns like FIFE (in Kansas over short grass) or BOREAS (in a boreal forest) [*Hall et al.*, 1992; *Betts and Ball*, 1995]. For example, *Hall et al.* [1992] calculated sensible heat fluxes from $T_s - T_{air}$ and tested this relationship with FIFE measurements. Assimilated in soil-vegetation-atmosphere (SVAT) models, skin temperatures help constrain the water and energy budget [e.g., *Lakshmi*, 2000].

[6] However, despite their recognized importance in a large number of applications, accurate measurements of surface skin temperatures over continents are not yet available for the whole globe, for clear and cloudy skies, with a time sampling adequate to resolve the diurnal cycle and to analyze synoptic, seasonal, and interannual variability.

[7] In situ surface skin temperature could be calculated from observations with an infrared radiometer, if the land surface emissivity was known: this measurement is not performed at weather stations and is not part of the conventionally measured data. Skin temperatures have been estimated from satellite infrared radiance observations. Instruments like AVHRR on board polar orbiters provide good spatial resolution with a limited time sampling (of the order of two overpasses per day per location) whereas radiometers on board geostationary weather satellites offer adequate sampling of the diurnal cycle but with a poorer spatial resolution. The main limitation of satellite infrared measurements of surface skin temperature is their inability to penetrate clouds, limiting them to clear conditions. Clouds not only cover more than half of the globe at a given time, they also alter the radiative energy exchanges, reducing surface insulation and increasing the downward longwave radiation. The magnitude and the sign of their net radiative effect depend upon the cloud characteristics and are quite variable [*Stephens and Webster*, 1981; *Stephens and Greenwald*, 1991; *Chen et al.*, 2001].

[8] The most extensive data set of land skin temperature available is produced at 3 hour intervals since 1983 over the globe, every 30 km, from polar and geostationary satellite infrared measurements by the International Satellite Cloud Climatology Project (ISCCP) [*Rossow and Schiffer*, 1999]. Analysis of the infrared measurements includes identification of clear scenes and correction for atmospheric effects (surface emissivity is assumed to be unity in this product). Based on infrared measurements, these results are biased to clear-sky conditions [*Rossow and Garder*, 1993]; but a statistical interpolation provides an estimate of the skin temperature for cloudy scenes.

[9] Other estimates exclusively based on polar orbiter infrared measurements have to supplement the limited time sampling with an analysis of the surface skin diurnal cycle inferred from model simulations and experiment campaigns [*Jin and Dickinson*, 1999] for clear pixels. To estimate surface skin temperatures from infrared measurements in cloudy conditions, *Jin* [2000] and *Jin and Dickinson* [2000] propose a technique that uses both neighboring (in time or space) clear pixels and the surface energy balance, combined with an adjustment derived from surface air temperature estimates for pixels under extended or quasi-permanent cloud cover. This method relies on parameterized relationships that are tuned to specific campaigns or to climatology, limiting the global application of the method.

[10] Only a limited number of studies have explored the potential of satellite microwave measurements for land surface temperature retrieval. Yet, microwave wavelengths being much less affected by clouds than the infrared are an attractive alternative in cloudy regions. *Njoku* [1995] concluded from simulations that land surface skin temperature could be retrieved from multichannel microwave observations with an accuracy of 2 to 2.5 K. *MacFarland et al.* [1990] investigated the correlation between observations with the Special Sensor Microwave /Imager (SSM/I) and "surface air" temperature measurements and suggested the use of multivariate regression of the microwave brightness temperatures to retrieve the "surface air" temperature. *Basist et al.* [1998] calculated "surface air" temperature from a linear regression with the SSM/I brightness temperatures, the regression coefficients being adjusted for variations in emissivity, using a simple land classification scheme. The algorithm has been further evaluated [*Williams et al.*, 2000] to produce a monthly-mean merged satellite-in situ near-surface temperature data set with a $1° \times 1°$ resolution. It is worth noting that these studies involving SSM/I correlate the microwave brightness temperature measurements to near-surface air temperatures, not to sur-

face skin temperatures, with the underlying assumption that the surface air and skin temperatures vary together which is approximately true for longer timescales.

[11] Recently, a neural network inversion scheme, including first guess information, has been developed to retrieve simultaneously the surface skin temperature (T_s), the atmospheric water vapor (*WV*), the cloud liquid water (*LWP*), and the surface emissivities (e_f) over land from SSM/I and infrared radiance observations [*Aires et al.*, 2001] using precalculated monthly-mean emissivities [*Prigent et al.*, 1997, 1998], ISCCP cloud and surface parameters [*Rossow and Schiffer*, 1999], and the meteorological analysis from NCEP (National Center for Environmental Prediction) [*Kalnay et al.*, 1996] as first guess information. The inversion method provides surface skin temperatures for each SSM/I observation over land with a theoretical rms error of 1.3 K in clear-sky and 1.6 K in cloudy scenes as well as revised surface emissivities in all channels. This study aims to evaluate the accuracy of the retrieved surface skin temperatures. First, the neural network method is described, with special emphasis on the post-facto detection of erroneous retrievals (section 2). Given the lack of in situ estimates of the surface skin temperature, the validity of the retrievals is evaluated through a comprehensive analysis of the differences expected between T_s and T_{air} as a function of diurnal (and seasonal) solar insulation, vegetation cover (moisture) and cloudiness variations (section 3). Section 4 concludes by discussing the value of producing a merged T_s and T_{air} data set to analyze the energy exchanges at the land-atmosphere interface.

2. A Neural Network Inversion Method

[12] A neural network inversion scheme, including first guess information, has been developed to retrieve T_s, *WV*, *LWP*, and e_f, over snow- and ice-free land from observations between 19 and 85 GHz measured by SSM/I [*Aires et al.*, 2001]. This neural method optimizes (we will see in which sense in section 2.1) the use of all the SSM/I channels and a priori information to constrain the inversion problem and retrieves simultaneously surface and atmospheric parameters that are consistent among themselves and with the satellite observations. The neural network is designed to analyze all the local statistical relationships in the learning database and benefits from them, even when the relationships are highly nonlinear. These relationships represent nonlinear correlations among the physical variables, among the observations (brightness temperatures), among the first guess quantities, and between the variables and the observations. All of these correlations constitute additional information which the neural network can exploit to improve its retrieval if such correlations are properly represented in the learning data set. In contrast, the variational assimilation scheme, in its usual implementation, does not take into account statistical information about nonlinear correlations among the variables. See *Aires et al.* [2001] for a comparison of the neural network and variational approaches.

2.1. Learning Algorithm With First Guess

[13] The neural network scheme is briefly presented here: Figure 1 summarizes the procedure, from the implementation of the learning data set to the operational use and the post-facto verification of the approach. The MultiLayer Perceptron (MLP) network is a nonlinear mapping model composed of distinct layers of neurons: The first layer S_0 represents the input $X = (x_i\ ;\ i \in S_0)$ of the mapping. The last layer S_L represents the output mapping $Y = (y_k;\ k \in S_L)$. The intermediate layers S_m $(0 < m < L)$ are called the "hidden layers". These layers are connected via neural links. We denote the parameters of these links as *W*.

[14] Usual neural network remote sensing inversion schemes use only satellite observations for the retrieval of the geophysical variables [e.g., *Krasnopolsky et al.*, 2000], but when an inverse problem is ill-posed, the solution can be non-unique and/or unstable. The use of a priori first guess information is important to reduce ambiguities because the chosen solution is then constrained to be physically more coherent. Statistically, this regularization avoids local minima during the learning process and speeds it up. Introduction of a priori first guess information as part of the input to the neural network was first proposed by *Aires et al.* [2001]. The neural transfer function is represented by:

$$\hat{y} = g_W\left(y^b, x^o\right) \tag{1}$$

where $\hat{y}$ is the retrieval (i.e., retrieved physical parameters), g_W is the neural network g with parameters *W*, y^b is the first guess for the physical parameters y, $x^o = RTM(y) + \eta$ are the observations simulated by a Radiative Transfer Model (RTM) applied to y, and η is the observation noise.

[15] The learning algorithm is an optimization technique that consists in estimating the parameters *W* of the neural network that minimize a cost function $C(W)$, often chosen to be the mean least squares error criterion. The term "mean" depends on the probability distribution functions of the physical observation and retrieved quantities. In this study, the least squares criterion has the following form

$$C(W) = \frac{1}{2}\int\int\int D_E\left(g_W\left(y^b, x^o\right), y\right)^2 \cdot P\left(y, x^o, y^b\right) \tag{2}$$

$$C(W) = \frac{1}{2}\int\int\int D_E(g_W(y+\varepsilon, x+\eta), y)^2 P(y) P_\eta(\eta) P_\varepsilon(\varepsilon), \tag{3}$$

where D_E is the Euclidean distance between y_k, the kth desired output component, and $\hat{y}_k$, the kth neural network output component, S_L is the output layer of the neural network, $P(y)$ is the probability distribution function of the physical variables y that depends on their natural variability, $P_\eta(\eta)$ is the probability distribution function of the observation noise η, and $P_\varepsilon(\varepsilon)$ is the probability distribution function of the first guess errors, $\varepsilon = y^b - y$.

[16] As explained by *Aires et al.* [2001], the quality criterion in equation (2) is very similar to the quality criterion used in variational assimilation. One of the main differences is that the neural network criterion in equation (2) involves the distribution $P(y)$. This illustrates the fact that the neural network simulates the inverse of the radiative transfer equation globally, once and for all, and uses the distribution $P(y)$ for this purpose. The neural network model

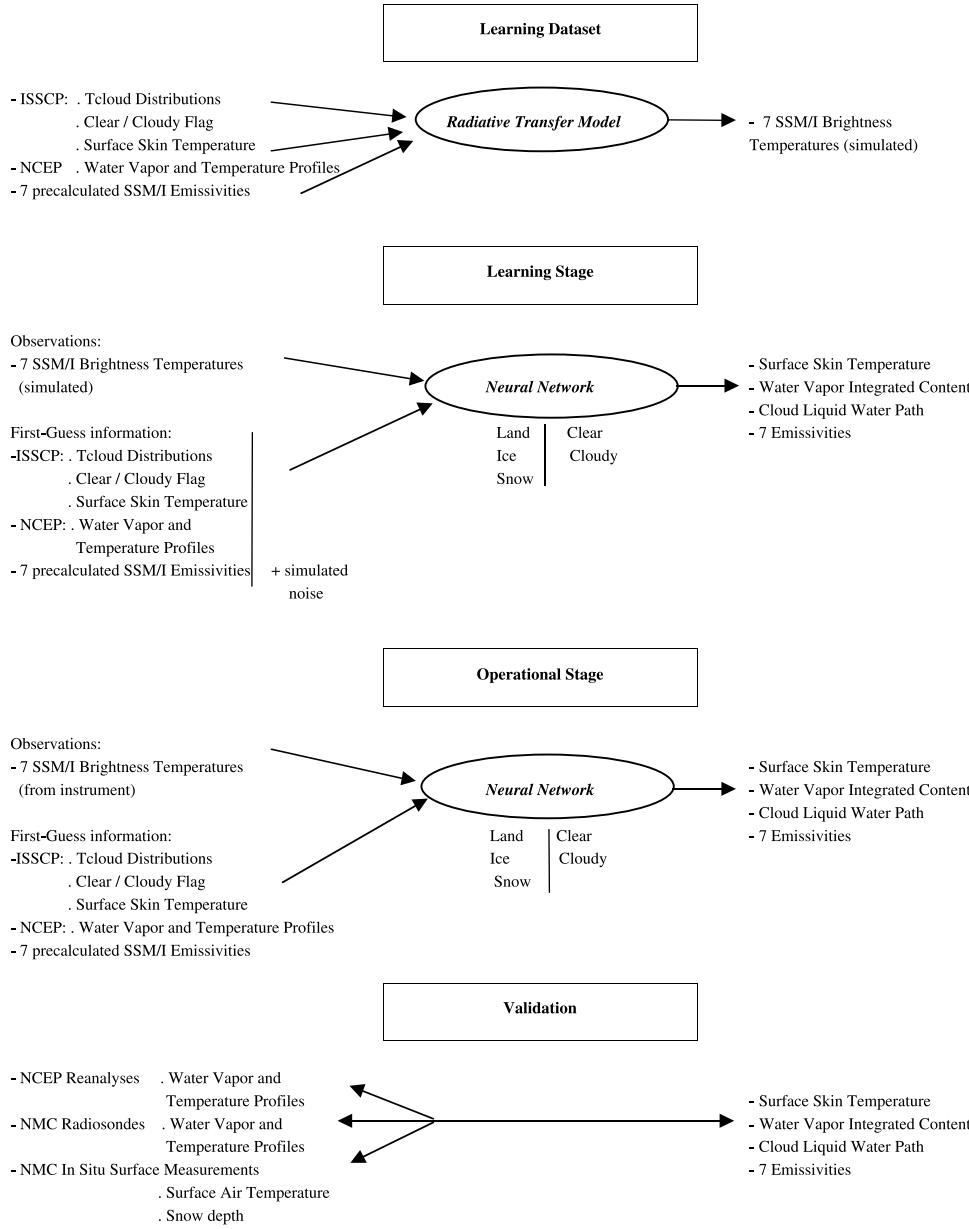

Figure 1. Schematic representation of the neural network inversion method.

is then valid for all observations (i.e., a global inversion). The variational assimilation model uses an inversion procedure for each observation (i.e., a local inversion).

[17] In practice, to minimize equation (2), we create a learning database $\mathcal{B} = \{(y^e, x^{oe}, y^{be}); e = 1,\ldots, E\}$ that samples as well as possible all the probability distribution functions in equation (2). Then, the practical criterion used during the learning stage is given by:

$$\tilde{C}(W) = \frac{1}{2E}\sum_{e=1}^{E} D_E\left(g_W\left(y^{be}, x^{oe}\right), y^e\right)\Big)^2. \qquad (4)$$

[18] First, to sample the probability distribution function, $P(y)$, we use actual observations of (y^e) in data sets that cover all natural combinations and their correlations and calculate $x^e = RTM(y^e)$ with the physical radiative transfer model (i.e., physical inversion). Alternatively we could obtain these relationships from a "sufficiently large" set of collocated and coincident values of x and y (i.e., empirical inversion). For sampling P_η, we need a priori information about the measurement noise characteristics; a physical noise model could be used, but if all we have is an estimation of the noise magnitude, we assume Gaussian distributed noise η that is not correlated among the measurements. To sample the first guess variability with respect to state y (i.e., sampling $P(y^b|y)$), we use a first guess data set $\{y^{be}; e = 1,\ldots, E\}$: this data set can be a climatological data set or a 6-hour prediction (which would have better statistics of errors, but would add model dependencies). The balance between reliance on the first guess and the direct measurements is then made automatically and optimally by the neural network during the learning stage. The classical error back-propagation algorithm, a gradient-descent algorithm

developed for the MLP [*Rumelhart et al.*, 1986], is used to minimize $(C)(W)$. It uses the gradient descent formula iteratively for a unique random sample in the learning data set. With some technical constraints not discussed here, the stochastic character of this optimization algorithm theoretically allows the optimization technique to reach the global minimum of the criterion instead of a local minimum reached with traditional gradient descent [*Duflo*, 1996]. At the optimum, the weight given by the learning process to the two sources of information in the input of the neural network (i.e., first-guess and observations) is determined in order to reach the best compromise.

2.2. Learning Database

[19] To better constrain (pose) the problem, we use the clear/cloudy flag information provided by the ISCCP data set to train two neural networks: One for clear scenes (NN1) and one for cloudy scenes (NN2). This specialization of the NNs facilitates the training of the neural network models. The architecture of the network NN1 is an MLP with 16 inputs coding the seven SSM/I observations, y^0, and the first guess, x_b (T_s, *WV*, and 7 e_f), 30 neurons in the hidden layer, and 9 neurons in the output layer coding the retrieval, x (T_s, *WV*, and 7 e_f). The network NN2 has one additional input, the cloud top temperature *Tc*, and one additional output, the cloud liquid water path (*LWP*). The number of neurons in the hidden layer is estimated by a heuristic procedure that monitors the generalization errors of the neural network as the configuration is varied. The procedure makes it possible to characterize the structure that will have the best performance on an independent data set.

[20] Two sources of information are used: (1) seven SSM/I brightness temperatures, and (2) a priori information of the state of the surface and atmospheric variables from ancillary data sets. A collection of SSM/I observations collocated and coincident with independent measurements of the parameters to be retrieved (T_s, *WV*, *LWP*, and the e_f) is not available. However, other estimates of T_s and *LWP* are available every 3 hours from ISCCP, NCEP provides *WV* analysis every 6 hours, and the land surface microwave emissivities are available as monthly estimates. As a consequence, brightness temperatures simulated by the radiative transfer model are used in the learning database instead of observations (see "Learning Dataset" in Figure 1). The learning database is made of ~22,500,000 samples, 55% of them corresponding to cloudy conditions. This simulated database is used only for the training of the neural network, not for the operational retrievals. The radiative transfer results are obtained using the values of T_s, *WV*, *LWP*, and e_f; to the extent that these data sets provide a proper distribution of the surface and atmospheric parameters, including their correlations, the neural network represents a global fit to the inverse of the radiative transfer function used for the simulation of the learning database. See *Aires et al.* [2001] for more details about the RTM and data sets.

[21] The SSM/I instrument on the Defense Meteorological Satellite Program polar satellites senses atmospheric and surface emissions at 19.35, 22.235, 37.0, and 85.5 GHz with both horizontal and vertical polarizations, except for 22.235 GHz which is vertical polarization only [*Hollinger et al.*, 1987]. An instrument evaluation has been performed by *Hollinger et al.* [1990] and an intersensor calibration has been completed by *Colton and Poe* [1999]. The radiometric noise is supposed to be Gaussian distributed. Errors in channels are supposed to be uncorrelated: the noise standard deviation of each channel brightness temperature is estimated to be 0.6 K. A more complex instrument noise model could be used in the neural network approach, even for non-Gaussian distributions, but these characteristics are the only ones available for SSM/I.

[22] The quality of the learning data set is essential to the quality of our retrieval scheme in operational mode. The quality of the learning data set depends upon the quality of the physical radiative transfer model used. It also depends upon the quality of the sampling of atmospheric situations. If the sampling representation of the learning data set is not good enough, this can introduce a bias in the results during the operational mode. However, we used a generalization data set, in practice a sub-part of the global data set available, not used during the learning stage, in order to control that the neural network is not overtrained (or overparameterized, i.e., where the parameters of the model are fitted too much on the learning data set) and in order to be able to generalize the neural network behavior on independent data sets.

[23] The temperatures and relative humidities for eight levels up to 300 mbar (middle and lower troposphere) are available from the NCEP reanalysis data set [*Kalnay et al.*, 1996], every 6 hours at a spatial resolution of 2.5° in latitude and longitude. For each location the atmospheric profile has been adjusted for consistency with the topography. The integrated water vapor *WV* is used as the first guess information. The standard deviation of the first guess error is taken to be 0.4 times the NCEP *WV* values, similar to the *WV* errors used for each humidity level by *Eyre et al.* [1993].

[24] In the ISCCP data, cloud parameters and related quantities are retrieved from visible (VIS ~0.6 μm wavelength) and infrared (IR ~11 μm wavelength) radiance provided by the set of polar and geostationary meteorological satellites [*Rossow and Schiffer*, 1999]. The ISCCP data set is used in this study to discriminate between clear and cloudy scenes (selecting NN1 or NN2) and to give first guess estimates of the cloud top and surface skin temperatures. The pixel level data set (the DX data set) is selected for its spatial sampling of about 30 km and its sampling interval of 3 hours [*Rossow et al.*, 1996]. If the ISCCP DX scenes are cloudy, a clear-sky compositing procedure is conducted within the ISCCP process to derive an estimate of the surface temperature. For each pixel every 5 days, separately at each diurnal phase, the IR measurements are compared to estimate the clear radiance that is called the clear-sky composite. In highly cloudy locations, the clear-sky estimate can be based on 15-day statistics. See *Rossow and Garder* [1993] and *Rossow et al.* [1996] for more details. If the ISCCP DX scenes are cloudy, a clear-sky compositing procedure is conducted within the ISCCP process to derive an estimation of the surface temperature (see *Rossow and Garder* [1993] for more details). The error associated with the surface temperature under all conditions is estimated to follow a Gaussian distribution with zero-mean and 4 K standard deviation [*Rossow and Garder*, 1993]. We apply a simple correction to the ISCCP T_s values to account for the surface emissivity at 11 μm wavelength. The correction is a simple fit to complete radiation calculation (because the corrections are generally small). The

variation of emissivity depends on surface type, especially vegetation, based on the database used in the GISS climate model [*Matthews*, 1983].

[25] For cloudy scenes, the cloud top temperature derived from IR measurements is added to the retrieval process as additional information to account for the changes in the emission temperature of the cloud and in the cloud liquid water absorption coefficient at microwave frequencies. The accuracy of the *LWP* retrieval varies widely with the cloud conditions, especially with cloud top temperature [*Prigent and Rossow*, 1999]. Thus knowledge of the cloud top temperature helps retrieve cloud liquid water path and the ISCCP DX cloud top temperature derived from IR measurements is used as a priori information. If the ISCCP DX cloud top temperature is >260 K, it is assumed that the cloud is composed solely of liquid water [*Lin and Rossow*, 1994] and the cloud water temperature is given by the ISCCP value. The error of the cloud top temperature for liquid water clouds is ~1.5 K [*Wang et al.*, 1999]. If the ISCCP cloud top temperature is <260 K, the upper portion of the cloud is probably composed of ice, but there is a possibility that this ice cloud obscures a liquid cloud [*Lin et al.*, 1998]. An analysis has been performed on global ISCCP DX data to estimate the statistical distribution of cloud top temperature of the liquid clouds over land for each 15° latitude zone for each month. Assuming that the distribution of liquid cloud top temperatures is not modified in the presence of an overlying ice cloud, the first guess liquid cloud top temperature is then drawn stochastically from the distribution of liquid cloud top temperature of the corresponding month and latitude zone to maintain random error characteristics [see *Aires et al.*, 2001].

[26] First guess a priori information for the microwave emissivities at each location is derived from the monthly mean emissivities previously estimated by *Prigent et al.* [1997, 1998, 2001]. Microwave emissivities were calculated by removing the contributions from the atmosphere, clouds, and rain using ancillary satellite data (ISCCP) and meteorological reanalysis (NCEP). Cloud-free SSM/I observations were first isolated with the help of collocated visible/infrared satellite observations (ISCCP data) and the cloud-free atmospheric contribution was calculated from an estimate of the local atmospheric temperature-humidity NECP profile. With the surface skin temperature derived from IR observations (ISCCP estimate), the surface emissivities were estimated for all the SSM/I channels and monthly mean values calculated with a spatial resolution of 0.25° × 0.25° at the equator [*Prigent et al.*, 1997, 1998]. The standard deviations of day-to-day variations of the retrieved emissivities within a month have been calculated for each channel and for each location and are used as estimates of first guess standard deviation error for these quantities. The surface contribution to the observed brightness temperatures is then calculated using the monthly mean emissivities assuming specular reflection at the surface.

[27] A direct radiative transfer model (RTM) adapted to the SSM/I channels is used to create the learning and testing databases required for the neural network inversion. The MPM 93 gaseous absorption model of *Liebe et al.* [1993] is adopted for all the SSM/I frequencies. Cloud absorption is calculated using the Rayleigh approximation which is valid for most non-precipitating liquid water clouds at SSM/I frequencies. The dielectric properties of liquid water are taken from *Manabe et al.* [1987]. Scattering by large particles is not considered, meaning that convective clouds and rain are not represented in the database.

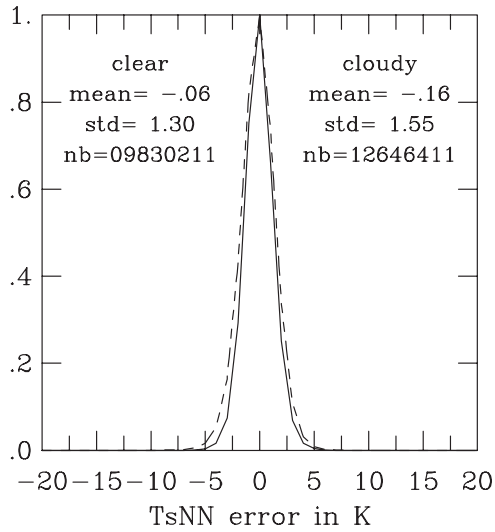

Figure 2. Histograms of the theoretical errors for T_s in Kelvin, separately for clear (solid line) and cloudy (dashed line) cases. The mean, the standard deviation, and the number of samples are also indicated.

[28] At the end of the training phase, the theoretical error of the neural network inversion is estimated from the learning database. Histograms of the errors in T_s are presented on Figure 2 for clear and cloudy cases separately. The rms error is of 1.3 and 1.6 K respectively for clear and cloudy cases, which is a significant improvement over the first guess error of 4 K.

2.3. A Posteriori Criterion to Test the Retrievals

[29] The neural inversion method has been applied to a year of SSM/I F10 and F11 observations (July 1992–June 1993) (see "Operational Stage" in Figure 1). Color maps of the retrieved products have been presented by *Aires et al.* [2001]. In the operational mode, the neural network scheme is computationally very efficient. Inversion of new observations only involves simple and rapid calculations of two matrix products and one pass through the logistic function of the neural network.

[30] The neural network technique also enables an analytical and fast calculation of the neural Jacobians also called the neural sensitivities. *Aires et al.* [2001] gave the global mean sensitivities for each retrieved parameter: they indicate the relative contribution of each input in the retrieval for a given output parameter. They showed that depending on the situation, the neural network adapts itself by using optimally all of the input parameters. Depending on the surface emissivity, T_s sensitivity changes from a larger sensitivity to *Tb* at 19 GHz for higher emissivities to a larger sensitivity to the *Tb* at 85 GHz and to the T_s first guess information for lower emissivities. The key is that the first guess guides the neural network to exploit the different spectral dependence signal and the emissivities for different surface types so that the temperature changes can be separated from emissivity changes.

[31] Neural network approaches have often been criticized for not being able to control the quality of their retrievals. This is incorrect. In the same way that iterative methods use a physical forward model to control their retrievals, as is done in the variational assimilation for example, it is also possible to use a direct model to check the quality of the neural network retrievals. In this study, we control the quality of the inverted parameters by comparing the observed brightness temperatures to simulated *Tbs* using the retrieved products.

[32] Such a comparison has been performed for 2 months of global SSM/I data over snow- and ice-free continental pixels. The histograms of the differences are presented for 19 and 85 GHz, for both horizontal and vertical channels (Figure 3). Results are separated for three cloud conditions (clear sky, cloudy with ISCCP cloud top temperature below 260 K, and cloudy with cloud top temperature above 260 K) and for three ranges of the emissivity at 19 GHz horizontal polarization e_{19H}. For the lower frequency channels, the rms errors are within the channel radiometric noise (0.60 K). The rms differences are larger for the horizontally polarized channels and they increase with frequency. This dependence is expected because surface emissivities are not only more variable for horizontal polarization, they are also smaller, increasing the contributions of atmospheric water vapor and cloud liquid water which produce most noticeable errors. In addition, the effect of clouds increases with increasing frequency. For cold clouds (cloud top temperature below 260 K), there is a noticeably broader right wing in the histograms at 85 GHz. For daytime observations, we checked that the pixels for which the differences between simulated and observed *Tbs* at 85 GHz are large are associated with large optical depths as estimated by ISCCP. Since the contribution of large ice and water precipitation-sized particles have not been considered in the inversion process in the RT model, the scattering by such particles, which decreases the brightness temperatures, is not accounted for, producing a population of pixels with simulated *Tbs* that are too large compared to the observed values for cold clouds and high frequencies. The explanation is confirmed by plotting the data again in Figure 3 but removing all clouds with ISCCP optical thickness larger than 30, which are associated with precipitation [*Lin and Rossow*, 1994]. In this case (not shown), the differences greater than 3 K are nearly all eliminated.

[33] Comparison of the observed and simulated brightness temperatures after inversion is not only a practical tool to flag erroneous retrievals and to analyze the behavior of the inverse model, but careful examination of the differences for each channel can diagnose the presence of rain and large ice particles. This will be the subject of a forthcoming study.

[34] In the following section, the differences between the observed and simulated brightness temperatures will be checked to remove the cases affected by precipitation, by applying a threshold of two standard deviations to each channel brightness temperature differences.

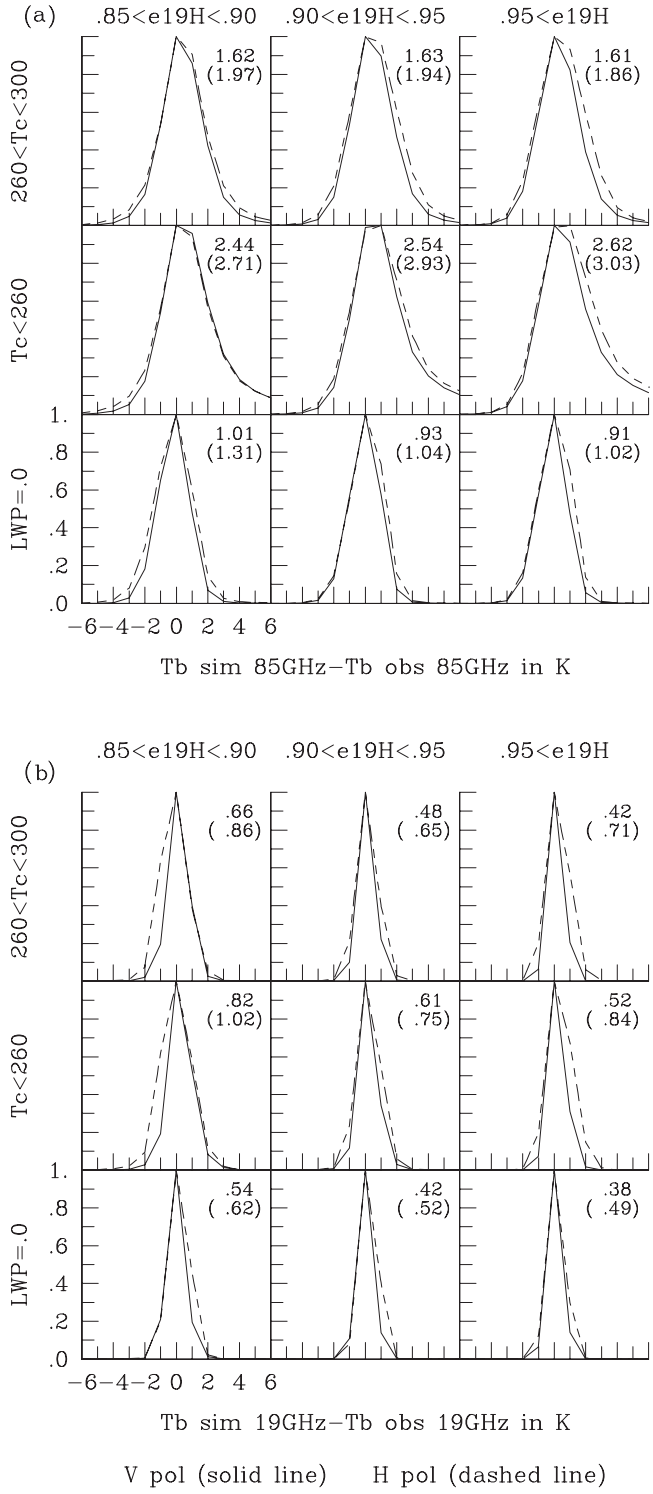

Figure 3. Histograms of the difference between the simulated *Tbs* after inversion and the observed *Tbs* (a) at 85 GHz and (b) at 19 GHz. Solid lines are used for vertical polarization, and dashed lines are used for horizontal. The rms errors are indicated for vertical (without parenthesis) and horizontal (with parenthesis) polarizations. Results are presented for three cloud conditions (clear sky, cloudy with ISCCP cloud top temperature below 260 K, cloudy with cloud top temperature above 260 K) and for three ranges of the emissivity at 19 GHz horizontal polarization e_{19H}.

3. Comparison Between Retrieved Surface Skin Temperatures and In Situ Air Temperatures

[35] Land surface temperature has been used to represent different variables depending on the application, leading to

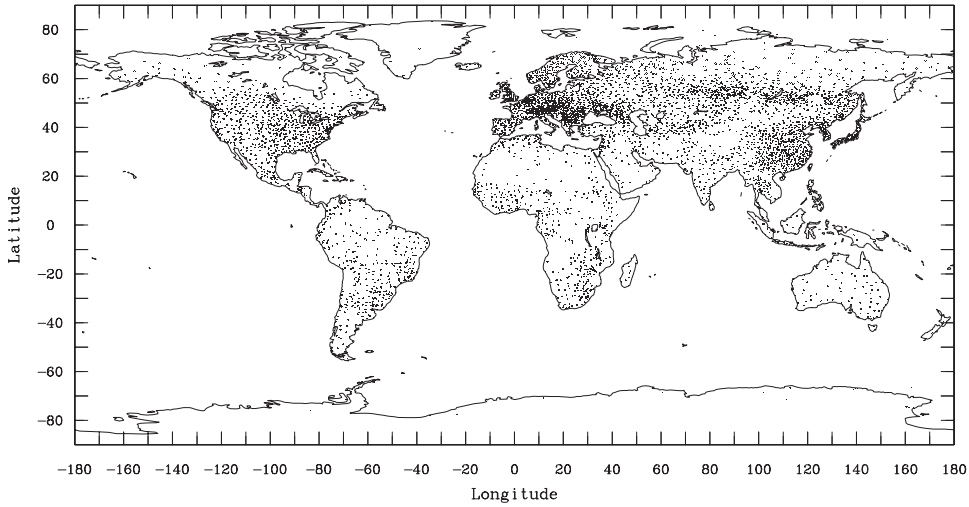

Figure 4. Map of the locations of coincident T_s and T_{air} observations.

confusion and misunderstandings. *Norman and Becker* [1995] attempted to clarify the terminology. In this study, T_s represents the surface skin temperature, also called the radiometric temperature. It is derived from IR remote sensing and as a consequence it is related to the measured radiance through the inverse of the Planck's law if the emissivity is known. T_{air} represents the thermodynamic temperature measured with a thermometer in the air between 1.5 and 3.5 m above the surface. Surface skin temperatures T_s are not part of the conventionally measured variables and as a consequence, validation of our results is a challenging task. Surface air temperatures T_{air} are routinely measured by surface weather stations and are distributed by the World Meteorological Organization (WMO) network. Measurements are performed with a sheltered thermometer located between 1.5 and 3.5 m above a flat, grassy, and well-ventilated surface. They are performed 4 times a day at 0:00, 6:00, 12:00, and 18:00 GMT. The precision of the reported values is 0.1°. Weather stations are concentrated in populated areas and are sparse or completely missing over large regions over the globe. In situ measurements and satellite estimates are considered coincident when they are within 20 km in space and within 2 hours in time. Figure 4 illustrates the locations of the coincidences between satellite observations and weather stations in this study.

[36] T_s and T_{air} are well correlated. A linear correlation coefficient of 0.88 is calculated for T_s and T_{air} coincidences over the globe for the whole year. The main T_s and T_{air} difference lies in their diurnal cycles. *Jin et al.* [1997] showed that skin and air temperatures differ the most at smaller spatial and temporal scales (regional and diurnal) and are very similar on monthly and hemispheric scales, except for a persistent seasonally and geographically varying bias. Solar radiation is the driving factor influencing the difference. The surface responds more rapidly to a changing solar forcing. The surface will warm up more quickly in the morning with the rising sun, inducing a positive $T_s - T_{air}$ difference during daytime, whereas it will also cool more rapidly at night, generating a negative $T_s - T_{air}$ difference.

[37] The fraction of absorbed solar radiation at the surface is determined by the surface albedo that depends upon the vegetation type and fractional cover, the albedo usually decreasing with increasing vegetation density. However, the dominant vegetation impact is associated with its effect on evaporative cooling, denser vegetation usually associated with more underlying soil moisture and with less restricted transpiration, that determines the partitioning of the incoming solar energy between temperature (longwave cooling and fluxes into the soil) and latent (and sensible) heat fluxes into the atmosphere [*Hall et al.*, 1995]. With decreasing soil and vegetation moisture, the evaporation rate decreases and the sensible heat flux increases, requiring larger $T_s - T_{air}$ differences during daytime.

[38] Clouds both reduce the incident solar flux and limit the outgoing infrared radiation, depending on the cloud macro-physical (altitude or temperature, optical thickness, and variability) and micro-physical properties (particle composition, shape, and size). *Stephens and Greenwald* [1991] discuss the sensitivity of T_s and the atmospheric vertical structure to cloud amount and form. *Chen et al.* [2001] showed that the effect of clouds on the surface radiation budget strongly depends on the cloud types.

[39] Air motion is another important force controlling the $T_s - T_{air}$ difference. Advection of an air mass with a different temperature than the local energy balance would establish can induce differences of $T_s - T_{air}$ that can be positive or negative depending on whether the advected air is colder or warmer than the surface. This effect will be especially important near midlatitude coasts.

[40] In the absence of in situ measurements to validate the retrieved T_s, the following analysis will attempt to examine the variations of the difference $T_s - T_{air}$ with the factors that are expected to affect it. All these factors being interconnected, it is difficult to isolate the influence of a single parameter. However, we will check that the expected behavior is observed, and, if that is the case, the errors on the retrieved T_s cannot be large.

[41] The sun-synchronous orbits of the DMSP satellites limit the comparisons of T_s and T_{air} on a diurnal basis. For the F10 and F11 satellites that provided data in 1992–1993, the ascending equatorial crossing times are at around 21:00 and 18:15 local time respectively (the F10 satellite did not

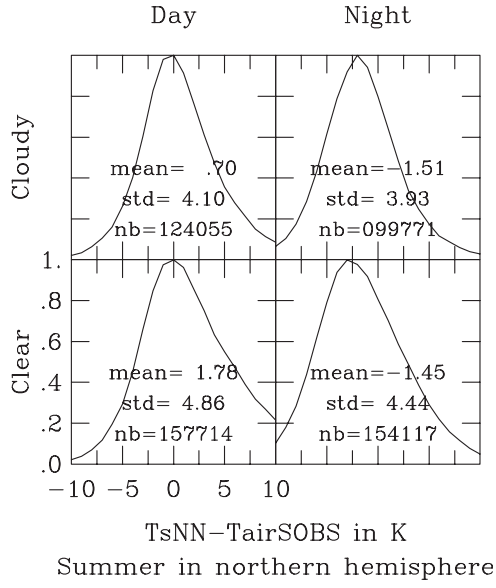

Figure 5. Histograms of the difference between T_s estimated from SSM/I observations and T_{air} in situ measurements. Results are presented for clear and cloudy scenes, separately for night and days, for summer months (June, July, August) in the Northern Hemisphere. The means and standard deviations of the differences are also indicated, along with the number of coincidences.

achieve the desired orbit and as a result the equator crossing time increases by approximately 45 minutes per year). Thus the satellites cross the equator in the early morning and late afternoon, far from noon when the difference in solar flux is maximum. Moreover a given area is always observed at about the same times, in the morning and in the evening, making it impossible to analyze the complete diurnal cycle at a given location. Attempts to study the diurnal variation of $T_s - T_{air}$ will inevitably involve different areas with different characteristics (solar incidence, water vapor content, and surface properties among others), introducing scatter in the results. The weather stations are unevenly distributed (Figure 4), so that the conjunction of their fixed sampling with the fixed overpassing times of the satellites worsens the sampling, concentrating the coincident measurements around 50 in latitude.

[42] Figure 5 shows the histograms of $T_s - T_{air}$ for summer (June, July, and August) over land in the Northern Hemisphere, separately for day and night and for clear and cloudy cases. For each histogram, the mean value, the standard deviation, and the number of pixels are specified. Although the satellite overpasses occur in the morning or in the late evening, the differences clearly exhibit the expected average behavior between nighttime and daytime. For clear conditions, $T_s - T_{air}$ is positive during daytime and negative during nighttime, consistent with the diurnal radiative forcing. T_s generally increases more rapidly that T_{air} under the influence of the solar flux during daytime but cools also more rapidly at night. During daytime, the mean difference is smaller for cloudy scenes as expected. During nighttime, the difference is slightly larger for cloudy scenes than for clear areas, which is contrary to expectations; however, the large standard deviations suggest that the results encompass a large variety of cases which are now further examined.

[43] The effect of the solar diurnal cycle is analyzed by separating the coincident T_s and T_{air} observations by local time. Vegetation and soil moisture are independent of the current meteorological and solar flux forcing, but they control the latent heat flux [*Hall et al.*, 1992]. Since soil moisture is not a variable that is routinely measured, the vegetation density is used as an indicator of the soil- and vegetation-available moisture. The data are sorted by vegetation density with the help of the *Matthews* [1983] vegetation and land use data set, compiled from a large number of published sources. Figure 6 presents the mean

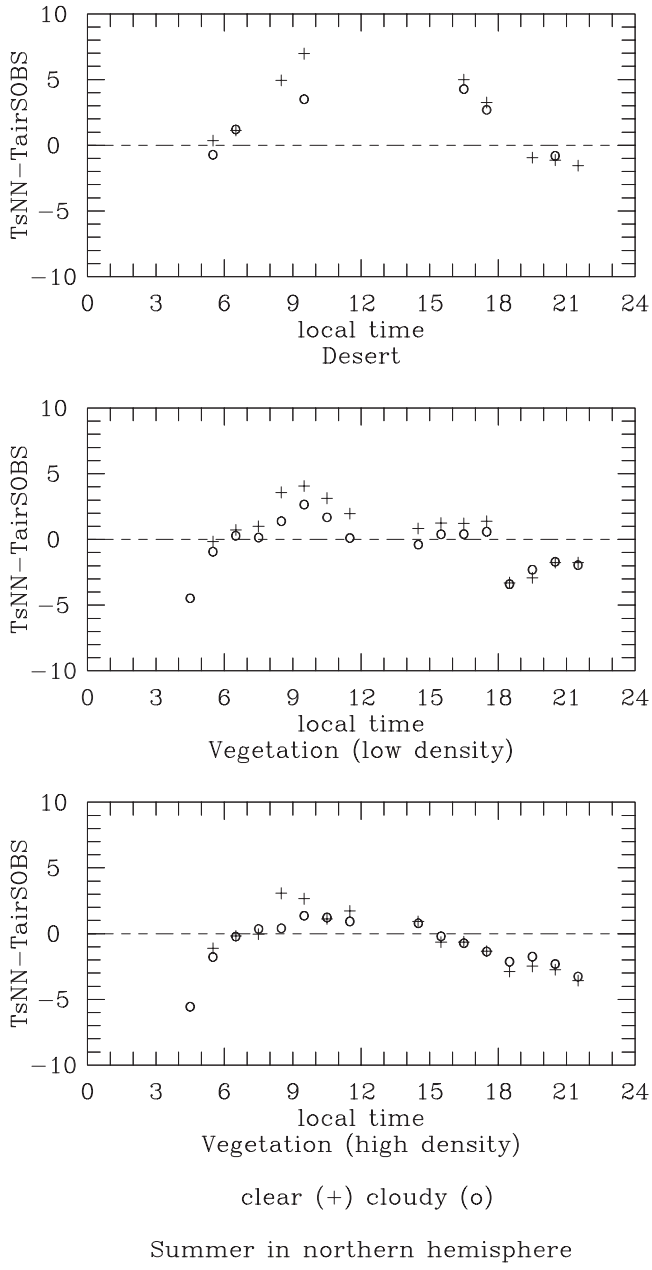

Figure 6. Mean $T_s - T_{air}$ for a given local time, presented for clear and cloudy scenes, separately for three types of vegetation, for summer months (June, July, August) in the Northern Hemisphere.

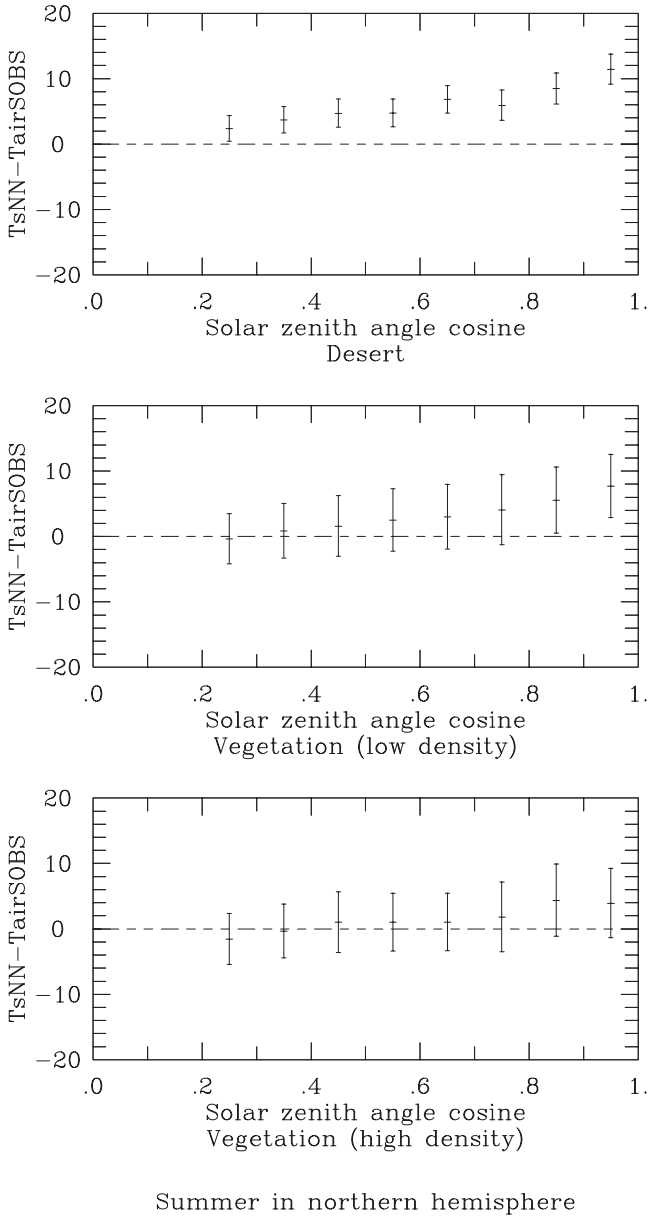

Figure 7. For each 0.1 step in solar zenith angle cosine, mean $T_s - T_{air}$. Results are presented for summer months (June, July, and August) in the Northern Hemisphere.

$T_s - T_{air}$ values for each hour (local time), for three classes of vegetation density, separately for clear and cloudy case for summer (June, July, and August) in the Northern Hemisphere. Most coincidences between satellite observations and in situ measurements occur in the early morning or in the evening, when the impact of the solar flux is smaller. During daytime for clear scenes, $T_s - T_{air}$ increases with decreasing vegetation density (moisture). In addition, there is a general increase of the difference from early morning to noon and then a decrease in the afternoon. The $T_s - T_{air}$ increase during daytime is especially large over desert, but there is no significant differences between the low and high density vegetation cases. *Betts and Ball* [1995] also observed similar soil moisture dependence from FIFE in situ measurements, with the $T_s - T_{air}$ daytime difference increasing with decreasing soil and vegetation moisture. They also noticed a 'saturation' effect for larger soil moisture, where the $T_s - T_{air}$ difference does not vary anymore with increasing moisture. For vegetated areas, the dependence with local time is less smooth than over desert because of the large variety of surfaces and latitudes included for a given local time. During daytime, the difference is larger for clear scenes than for cloudy pixels. As expected, the opposite is true when the sun declines, with the cloud cover preventing the cooling of the surface.

[44] The dominant influence of the solar zenith angle on the $T_s - T_{air}$ during daytime is further illustrated on Figure 7 where the difference is plotted versus the cosine of the solar zenith angle for clear scenes. The mean $T_s - T_{air}$ increases almost linearly with the solar zenith angle cosine, the magnitude increasing as vegetation density decreases.

[45] We also examined data from other seasons. The wintertime results are confused by the presence of snow (which we consider in a separate paper). If we limit the wintertime results to snow-free areas the number of samples is smaller and generally limited to lower latitudes. Nevertheless, we found the expected behavior, especially under clear conditions, with the daytime $T_s - T_{air}$ positive but smaller that in summertime and the nighttime difference negative, more so than in summertime.

[46] During daytime, clouds limit the amount of solar flux impinging on the Earth surface; the magnitude of their effect depends upon optical thickness and cloud amount [*Stephens and Greenwald*, 1991; *Hartmann et al.*, 1996; *Chen et al.*, 2001]. In addition, clouds limit the outgoing long-wave flux; the magnitude of their effect dependent mostly on cloud base height (temperature) and cloud amount [*Stephens and Greenwald*, 1991; *Hartmann et al.*, 1996; *Chen et al.*, 2001]. The warming effect of the clouds through their trapping of long-wave radiation is easier to see at night, when the solar flux effect is absent. For cloudy scenes during daytime, Figure 8 (left) presents for each hour (local time) and each 2 K difference in $T_s - T_{air}$ the mean value of the ISCCP optical thickness. For each local time, the mean $T_s - T_{air}$ difference is also added (black asterisks). For a given local time, as expected, $T_s - T_{air}$ generally decreases with increasing optical thickness. During daytime there is no obvious behavior differences between warm and cold clouds (not shown). For cloudy scenes during nighttime, the mean value of the cloud top temperature is presented, for each hour (local time) and each 2 K difference in $T_s - T_{air}$ (Figure 8, right). The cloud top temperature is derived from the ISCCP data set. The effective radiative temperature of the cloud is not equal to its cloud top temperature, but this is the only quantity that is observable from satellite and a good correlation is expected between these two temperatures [*Wang et al.*, 1999]. For a given local time, $T_s - T_{air}$ increases with increasing cloud top temperature, i.e., warmer clouds tend to prevent long-wave radiation escape at night more than cold clouds.

[47] We have demonstrated that solar illumination, moisture, and cloud cover have the expected effects on the $T_s - T_{air}$ differences. However, large standard deviations have been observed around the mean values and we will now show the impact of the weather on the differences.

[48] The radiatively driven differences in T_s and T_{air} exhibit a marked diurnal cycle. In order to remove most

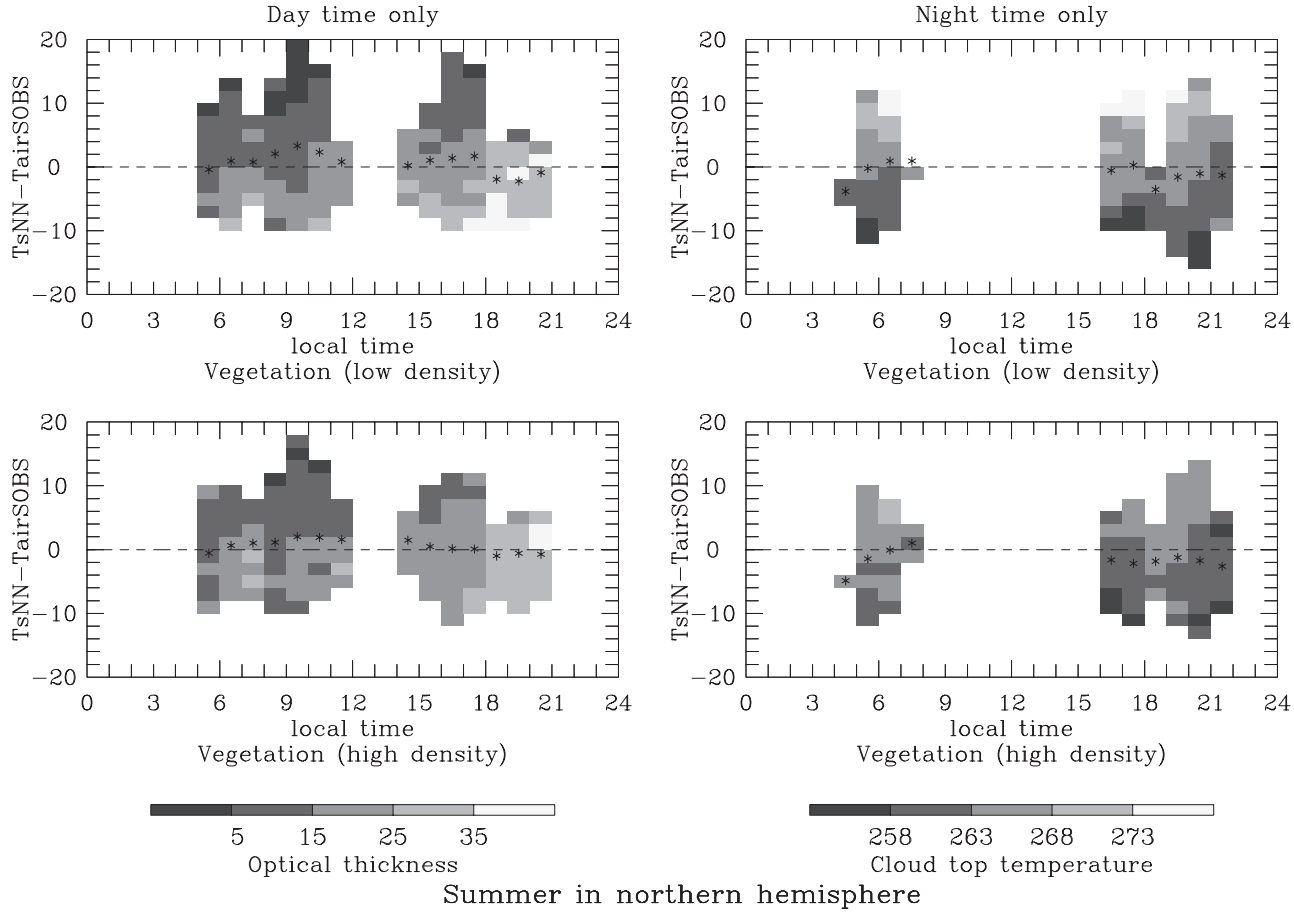

Figure 8. (left) For cloudy scenes during daytime, mean value of the ISCCP optical thickness for each hour (local time) and each 2 K difference in $T_s - T_{air}$. For each local time, the mean difference is also added (asterisks). (right) For cloudy scenes during nighttime, the mean value of the cloud top temperature, for each hour (local time) and each 2 K difference in $T_s - T_{air}$.

of this variability and to isolate the variations that are associated with weather, monthly mean diurnal cycles are calculated from each data set separately (the T_s and the T_{air} data sets) and are subtracted from each single estimate, resulting in temperature deviations from the monthly mean diurnal cycles for both T_s and T_{air}. Figure 9 shows the histograms of the collocated differences between their two temperature deviations, cumulated for July and December. The difference shows no bias and a standard deviation of ~2.9 K. We checked that the standard deviation increases from tropical areas to midlatitude regions: from 2.42 K for the 0 N–30 N latitude zone to 2.95 K for the 40 N–60 N area. In midlatitude regions, advection of air masses with a different temperature than the local energy balance would establish can induce large differences of both signs between T_s and T_{air}, locally and momentarily. We also checked that this scatter related to the synoptic variability is larger in winter than in summer and exhibits different behaviors near east coast and west coasts.

[49] The temperature deviations of the two data sets are compared, for various locations. Figure 10 shows examples of time series of T_s and T_{air} synoptic deviations for 3 locations and for 2 months. Cloudy conditions are flagged. The three locations represent different environments: the

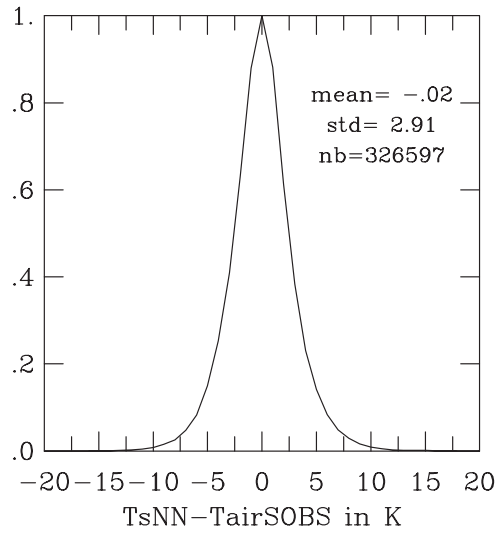

Figure 9. Histogram of the difference between T_s and T_{air} once the diurnal cycle has been removed from the two data sets separately. Results are presented cumulated for July and December. The mean, the standard deviation, and the number of pixels are indicated.

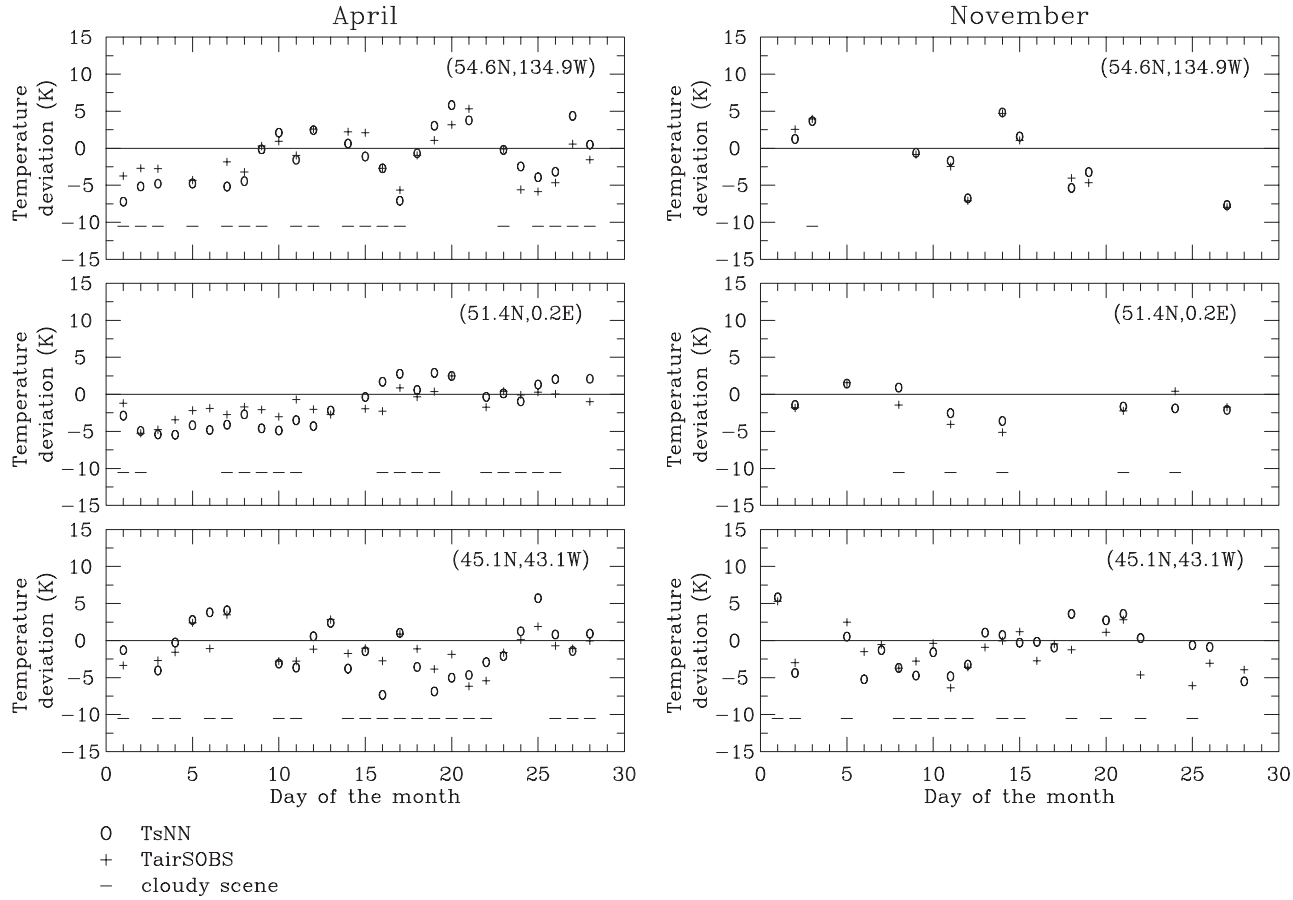

Figure 10. Time series of T_s and T_{air} deviations from the monthly mean diurnal cycle for three locations and for 2 months. Cloudy conditions are flagged.

first example (45.1 N, 43.1 W) is located in the Russian steppes, between the Black and the Caspian seas, north of the Caucasus mountains, the second one (51.4 N, 0.2 E) is in the west suburbs of London, and the last location (54.6 N, 134.9 W) is in a forested area close to the east coast of Russia on the sea of Okhotsk. The T_s and T_{air} deviations from the monthly mean diurnal cycle are both driven by the relative synoptic variability and the time series show good agreement, regardless of the environment. Rapid jumps in the temperatures are generally well captured (see especially the third location). It is important to notice that the presence of clouds does not degrade the agreement between the two variables, confirming the validity of the T_s estimate in cloudy conditions.

[50] The overall standard deviation of 3 K (Figure 9) contains contributions from retrieval error and imperfections in the validation data, whether it be mismatches in the spatial and temporal matchup, actual errors in the validation data set or representivity errors. Note that the post-facto check on the accuracy of the retrieval (Figure 3 with precipitation cases removed) suggests an error on *Tb* of 1–2 K, about twice the instrumental noise level at high frequency. Therefore the actual retrieval error will be less than 3 K. As the theoretical error for an optimal system is 1.5 K the true retrieval error will lie between 1.5 K and 3 K. The errors are therefore below those of the ISCCP data set for cloudy conditions [*Rossow and Garder*, 1993]. This implies that microwave land surface temperature estimates in cloudy conditions can make a contribution to characterizing land surface process modeling.

4. Conclusion

[51] A neural network inversion scheme including first guess information has been applied to the retrieval of surface temperature, atmospheric water vapor, cloud liquid water, and surface emissivities over land from SSM/I. All the parameters are simultaneously retrieved, insuring internal coherence between them. This work focuses on the validation of the surface skin temperature T_s. In the absence of routine in situ surface skin temperature measurements, our T_s values are evaluated by comparison to the surface air temperatures, T_{air}, that are conventionally measured by the meteorological station network. The $T_s - T_{air}$ difference shows all of the expected variations with solar flux, soil characteristics, and cloudiness. During daytime the $T_s - T_{air}$ difference is driven by the solar short-wave flux. The difference is positive and increases with increasing solar flux. With decreasing soil and vegetation moisture, the evaporation rate decreases, increasing the sensible heat flux and thus requiring larger $T_s - T_{air}$ differences. Nighttime $T_s - T_{air}$ differences are governed by the long-wave radiation balance, with T_s usually close to or lower than T_{air}. The presence of clouds dampens all of the differences.

After suppression of the variability associated to the diurnal solar flux variations, the T_s and T_{air} data sets show very good agreement in their synoptic variability, even for cloudy cases, with no bias and a global rms difference of $\lesssim$3 K. This value is an upper limit on the retrieval errors because it includes errors in the in situ measurements as well as errors related to imperfect time and space collocations between the satellite and in situ measurements.

[52] SSM/I observations have already been used to infer T_{air}, although these observations are more sensitive to T_s. The correlation of T_s and T_{air} variations is quite high, so that the variability of T_{air} can be estimated from microwave variability, but this requires 'tuning' of the results for all locations, not just for one region, because the biases are regionally and seasonally dependent. The quantitative accuracy of using microwaves as estimates of T_{air} is given by the $\lesssim$3 K difference we found for synoptic, in addition to a smaller or larger range for diurnal, depending on region and season. However, the microwave observations cannot be used to monitor climate variations of T_{air}: Changes in climate might also involve changes in the average difference between T_s and T_{air} because surface and atmospheric moisture as well as clouds might also change.

[53] Microwave land surface skin temperature retrieval is a very promising complement to infrared estimates, with the significant advantage that it is effective whatever the weather conditions, clear or cloudy. However, because of the larger emissivity variations in the microwave than in the infrared, a combined analysis is required to isolate the temperature variations accurately. *Ts* measurement campaigns have to be conducted in various environments, including an adequate sampling of the diurnal cycle under different cloud conditions. This is the only way to validate the retrieved products.

[54] Over ocean, the sea surface temperature is known to play a major role in forcing the atmosphere and there are attempts to create a hourly sea surface skin temperature for the calculation of the fluxes of sensible and latent heat [*Zeng et al.*, 1999]. Over land, even stronger and more complex interactions are expected due to the large T_s diurnal cycle and the limited availability of soil moisture. Energy and water exchanges at the land-atmosphere interface are largely controlled by the skin temperatures and the soil moisture. Measurements of the skin temperatures, with time resolution high enough to resolve the diurnal cycle under all synoptic conditions, and covering a long enough period to examine how different seasonal and interannual conditions affect them, are required to study the energy and water exchange processes at the land-atmosphere interface. In addition, satellite microwave observations can not only help provide more complete T_s time series, they have also shown a promising sensitivity to soil moisture [*Lakshmi et al.*, 1997; *Owe et al.*, 1999; *Vinnikov et al.*, 1999], another key parameter at the land-atmosphere interface.

[55] A joint analysis of 10 years of microwave SSM/I satellite measurements and ISCCP products is now under way to obtain an all-weather time record of land surface skin temperatures. Future plans include the merging of the resulting global satellite observations of land surface skin temperature with global surface weather observations of near-surface air temperature, humidity, and winds to produce a data set that can be used to study the diurnal, synoptic, and seasonal variations of land-atmosphere energy and water exchanges.

[56] **Acknowledgments.** The authors would like to thank Ting Chen for his thoughtful comments. They are grateful to Ralph Karow and Cindy Pearl for their help in processing the data. They also thank two anonymous reviewers for their careful reading of the manuscript. The Global Hydrology Data Center (NASA/Marshall) provided the SSM/I data set. NCEP Reanalysis data were obtained from the NOAA-CIRES Climate Diagnostics Center, Boulder, Colorado, USA, from their Web site at http://www.cdc.noaa.gov/. This work was partly supported by special funding provided by Dr. Robert J. Curran and Dr. Donald Anderson, NASA Climate and Radiation Program.

References

Aires, F., C. Prigent, W. B. Rossow, and M. Rothstein, A new neural network approach including first guess for retrieval of atmospheric water vapor, cloud liquid water path, surface temperature, and emissivities over land from satellite microwave observations, *J. Geophys. Res.*, *106*, 14,887–14,907, 2001.

Basist, A., N. C. Grody, T. C. Peterson, and C. N. Williams, Using the Special Sensor Microwave/Imager to monitor land surface temperatures, wetness, and snow cover, *J. Atmos. Sci.*, *37*, 888–911, 1998.

Betts, A. K., and J. H. Ball, The FIFE surface diurnal cycle climate, *J. Geophys. Res.*, *100*, 25,679–25,693, 1995.

Betts, A. K., J. H. Ball, A. C. M. Beljaars, M. J. Miller, and P. A. Viterbo, The land surface-atmosphere interaction: A review based on observational and global modeling perspectives, *J. Geophys. Res.*, *101*, 7209–7225, 1996.

Carlson, T. N., J. K. Dood, S. G. Bejamin, and J. N. Cooper, Satellite estimation of the surface energy balance, moisture availability and thermal inertia, *J. Appl. Meteorol.*, *20*, 67–87, 1981.

Chen, T., W. B. Rossow, and Y. Zhang, Radiative effects of cloud-type variations, *J. Clim.*, *13*, 264–286, 2001.

Colton, M. C., and G. A. Poe, Intersensor calibration of DMSP SSM/I's: F-8 to F-14, 1987–1997, *IEEE Trans. Geosci. Remote Sens.*, *37*, 418–439, 1999.

Duflo, M., Algorithmes stochastiques, in *Mathématiques et Applications*, pp. 154–162, Springer-Verlag, New York, 1996.

Eyre, J. R., G. A. Kelly, A. P. MacNelly, E. Anderson, and A. Persson, Assimilation of TOVS radiance information through one-dimensional variational analysis, *Q. J. R. Meteorol. Soc.*, *119*, 1427–1463, 1993.

Garrat, J. R., Observed screen (air) and GCM surface/screen temperatures: Implications for outgoing longwave fluxes at the surface, *J. Clim.*, *8*, 1360–1368, 1995.

Hall, F. G., K. F. Huemmrich, S. J. Goetz, P. J. Sellers, and J. E. Nickeson, Satellite remote sensing of surface energy balance: Success failures, and unresolved issues in FIFE, *J. Geophys. Res.*, *97*, 19,061–19,089, 1992.

Hall, F. G., J. R. Townshend, and E. T. Engman, Status of remote sensing algorithms for estimation of land surface state parameters, *Remote Sens. Environ.*, *51*, 138–156, 1995.

Hartmann, D. L., M. E. Ockert-Bell, and M. L. Wylie, The effect of cloud type on Earth's energy balance: Global analysis, *J. Clim.*, *5*, 1281–1304, 1996.

Hollinger, J. P., R. Lo, G. Poe, R. Savage, and J. Pierce, Special Sensor Microwave/Imager user's guide, Naval Res. Lab., Washington, D. C., 1987.

Hollinger, J. P., J. L. Pierce, and G. A. Poe, SSM/I instrument evaluation, IEEE Trans, *Geosci. Remote Sens.*, *28*, 781–790, 1990.

Idso, S. B., T. J. Schmugge, R. D. Jackson, and R. J. Reginato, The utility of surface temperature measurements for the remote sensing of soil water status, *J. Geophys. Res.*, *80*, 3044–3049, 1975.

Jackson, R. D., R. J. Reginato, and S. B. Idso, What canopy temperature: A practical tool for evaluating water requirements, *Water Resour. Res.*, *13*, 651–656, 1977.

Jin, M., Interpolation of surface radiative temperature measured from polar orbiting satellites to a diurnal cycle: 2. Cloudy-pixel treatment, *J. Geophys. Res.*, *105*, 4061–4076, 2000.

Jin, M., and R. E. Dickinson, Interpolation of surface radiative temperature measured from polar orbiting satellites to a diurnal cycle: 1. Without clouds, *J. Geophys. Res.*, *104*, 2105–2116, 1999.

Jin, M., and R. E. Dickinson, A generalized algorithm for retrieving cloudy sky skin temperature from satellite thermal infrared radiances, *J. Geophys. Res.*, *105*, 27,037–27,047, 2000.

Jin, M., R. E. Dickinson, and A. M. Vogelmann, A comparison of GCM2-BATS skin temperature and surface-air temperature with satellite and surface observations, *J. Clim.*, *10*, 1505–1524, 1997.

Kalnay, E., et al., The NCEP/NCAR 40-year reanalysis project, *Bull. Am. Meteorol. Soc.*, *77*, 437–470, 1996.

Krasnopolsky, V. M., W. H. Gemmill, and L. C. Breaker, A neural network multi-parameter algorithm SSM/I ocean retrievals: Comparisons and validations, *Remote Sens. Environ.*, *73*, 133–142, 2000.

Lakshmi, V., A simple surface temperature assimilation scheme for use in land surface models, *Water Resour. Res.*, *36*, 3687–3700, 2000.

Lakshmi, V., E. F. Wood, and B. J. Choudhury, Evaluation of Special Sensor Microwave/Imager satellite data for regional soil moisture estimation over the Red River Basin, *J. Appl. Meteorol.*, *36*, 1309–1328, 1997.

Legates, D. R., and C. J. Willmott, Mean seasonal and spatial variability in global surface air temperature, *Theor. Appl. Climatol.*, *41*, 11–21, 1990.

Liebe, H. J., G. A. Hufford, and M. G. Cotton, Propagation modeling of moist air and suspended water/ice particles at frequencies below 1000 GHz, paper presented at Specialist Meeting of the Electromagnetic Wave Propagation Panel, Adv. Group for Aerospace Res. and Dev., Palma de Mallorca, Spain, 1993.

Lin, B., and W. B. Rossow, Observations of cloud liquid water path over oceans: Optical and microwave remote sensing methods, *J. Geophys. Res.*, *99*, 20,907–20,927, 1994.

Lin, B., B. A. Wielicki, P. Minnis, and W. B. Rossow, Estimation of water cloud properties from satellite microwave, infrared and visible measurements in oceanic environments: 1. Microwave brightness temperature simulations, *J. Geophys. Res.*, *103*, 3873–3886, 1998.

MacFarland, J. M., R. L. Miller, and C. M. U. Neale, Land surface temperature derived from the SSM/I passive microwave brightness temperatures, *IEEE Trans. Geosci. Remote Sens.*, *28*, 839–845, 1990.

Manabe, T., H. J. Liebe, and G. A. Hufford, Complex permittivity of water between 0 and 30 THz, paper presented at 12th International Conference on Infrared and Millimeter Waves, IEEE, Orlando, Fla., 1987.

Matthews, E., Global vegetation and land use: New high-resolution data bases for climate studies, *J. Clim. Appl. Meteorol.*, *22*, 474–486, 1983.

Njoku, E. G., Surface temperature estimation over land using satellite microwave radiometry, in *Passive Microwave Remote Sensing of Land-Atmosphere Interaction*, edited by B. J. Choudhury et al., pp. 509–530, Vsp, Utrecht, Netherlands, 1995.

Norman, J. M., and F. Becker, Terminology in thermal infrared remote sensing of nature surfaces, *Agric. For. Meteorol.*, *77*, 153–166, 1995.

Owe, M., A. A. Van de Griend, R. de Jeu, J. J. de Vries, E. Seyhan, and E. T. Engman, Estimating soil moisture from satellite microwave observations: Past and ongoing projects, and relevance to GCIP, *J. Geophys. Res.*, *104*, 19,735–19,742, 1999.

Price, J. C., Thermal inertia mapping: A new view of the Earth, *J. Geophys. Res.*, *82*, 2582–2590, 1977.

Prigent, C., and W. B. Rossow, Retrieval of surface and atmospheric parameters over land from SSM/I: Potential and limitations, *Q. J. R. Meteorol. Soc.*, *125*, 2379–2400, 1999.

Prigent, C., W. B. Rossow, and E. Matthews, Microwave land surface emissivities estimated from SSM/I observations, *J. Geophys. Res.*, *102*, 21,867–21,890, 1997.

Prigent, C., W. B. Rossow, and E. Matthews, Global maps of microwave land surface emissivities: Potential for land surface characterization, *Radio Sci.*, *33*, 745–751, 1998.

Prigent, C., A. Aires, W. B. Rossow, and E. Matthews, Joint characterization of the vegetation by satellite observations from visible to microwave wavelengths: A sensitivity analysis, *J. Geophys. Res.*, *106*, 20,665–20,685, 2001.

Rossow, W. B., and L. C. Garder, Validation of ISCCP cloud detections, *J. Clim.*, *6*, 2370–2393, 1993.

Rossow, W. B., and R. A. Schiffer, Advances in understanding clouds from ISCCP, *Bull. Am. Meteorol. Soc.*, *80*(11), 2261–2287, 1999.

Rossow, W. B., A. W. Walker, D. E. Beuschel, and M. D. Roiter, International Satellite Cloud Climatology Project (ISCCP): Document on new cloud datasets, NASA Goddard Inst. for Space Stud., New York, 1996.

Stephens, G. L., and T. J. Greenwald, The Earth's radiation budget and its relation to atmospheric hydrology: 2. Observations of cloud effects, *J. Geophys. Res.*, *96*, 15,325–15,340, 1991.

Stephens, G. L., and P. J. Webster, Clouds and climate: Sensitivity of simple systems, *J. Atmos. Sci.*, *38*, 235–247, 1981.

Vinnikov, K. Y., A. Robock, S. Qiu, J. K. Entin, M. Owe, B. J. Choudhury, S. E. Hollinger, and E. G. Njoku, Satellite remote sensing of soil moisture in Illinois, United States, *J. Geophys. Res.*, *104*, 4145–4168, 1999.

Wang, J., W. B. Rossow, T. Uttal, and M. Rozendaal, Variability of cloud vertical structure during ASTEX observed from a combination of rawinsonde, radar, ceilometer, and satellite, *Mon. Weather Rev.*, *127*, 2484–2490, 1999.

Williams, C. N., A. Basist, T. C. Peterson, and N. Grody, Calibration and verification of land surface temperature anomalies derived from the SSM/I, *Bull. Am. Meteorol. Soc.*, *81*, 2141–2156, 2000.

Zeng, X., M. Zhao, R. E. Dickinkson, and Y. He, A multiyear hourly sea surface skin temperature data set derived from the TOGA TAO bulk temperature and wind speed over the tropical Pacific, *J. Geophys. Res.*, *104*, 1525–1536, 1999.

F. Aires and W. B. Rossow, NASA Goddard Institute for Space Studies, 2880 Broadway, New York, NY 10025, USA. (faires@giss.nasa.gov; wrossow@giss.nasa.gov)

C. Prigent, LERMA, Observatoire de Paris, 61, avenue de l'Obseravtoire, 75014 Paris, France. (catherine.prigent@obspm.fr)